Modeling of hydraulic fracturing using a porous-media phase-field approach with reference to experimental data

Yousef Heider[a,d,*], Sönke Reiche[b], Philipp Siebert[c], Bernd Markert[a]

[a] Institute of General Mechanics, RWTH Aachen University, Templergraben 64, 52062 Aachen, Germany
[b] Institute for Applied Geophysics and Geothermal Energy, RWTH Aachen University, Mathieustr. 10, 52074 Aachen, Germany
[c] Chair of Geotechnical Engineering, RWTH Aachen University, Mies-van-der-Rohe-Str. 1, 52074 Aachen, Germany
[d] Department of Civil Engineering and Engineering Mechanics, Columbia University, New York, NY 10027, USA

ABSTRACT

The underlying study introduces a numerical modeling framework and a comparison with experimental data of hydraulic fracture in dense low-permeable brittle rocks. This is based on the continuum theory of porous media (TPM) extended by a diffusive phase-field modeling (PFM) approach. Proceeding with a biphasic material consisting of a solid and a fluid phase, the mechanical behaviors, such as the solid deformation and the pore-fluid flow are described using the macroscopic TPM. The hydraulically-driven cracking is modeled in the sense of brittle fracture using the energy-minimization-based PFM procedure, which employs a scalar-valued phase-field variable to approximate the sharp edge of the crack by a diffusive transition zone. The combined TPM-PFM approach allows to model additional related phenomena, such as the permanent local changes of the intrinsic permeability and the volume fractions of the constituents in the crack and at the crack-domain interface. For the purpose of model calibration, simulations of 2D and 3D initial-boundary-value problems (IBVP) are introduced and compared to laboratory experiments on hydraulic fracturing. The results show that experimentally-derived pressure curves and estimated fracture lengths are well predicted in the proposed numerical simulations. It is also worth mentioning that the TPM-PFM approach can straightforwardly be implemented in common continuum finite element packages, allowing for a robust solution of hydraulic fracture problems.

1. Introduction

The topics of crack initiation and propagation in solid and porous materials have attracted many theoretical, experimental and numerical studies in the last few decades. On the one hand, the importance of these topics stems from their great relevance to safety assessment and reliability of structures. On the other hand, induced cracking is used in energy and environmental engineering as a tool to improve the efficiency of energy-related constructions. For instance, hydraulic fracturing is applied in enhanced geothermal systems (EGS) through injection of high-pressure water into deep dense crystalline rock layers with very low permeability and high temperature in order to enhance the rock's permeability. This helps increasing the system's efficiency and, thus, production of electricity at lower costs. Hydraulic fracturing (fracking) is also applied in petroleum engineering using pressurized liquids with chemical additives to extract unconventional forms of natural gas including coal seam gas, shale and tight gas. In spite of the great economical benefits of hydraulic fracturing, opponents to hydraulic fracturing refer to possible triggering of earthquakes, especially in the case of application to enhanced

* Corresponding author at: Institute of General Mechanics, RWTH Aachen University, Templergraben 64, 52062 Aachen, Germany.
  E-mail address: heider@iam.rwth-aachen.de (Y. Heider).

geothermal systems. More critics emerge also from the possible increase of air and noise pollution, or contamination of ground and surface water when using chemical additives in the fracking process to obtain, e.g., shale gas. The latter points show the importance of deep understanding of the cracking processes and the need to develop accurate and efficient mathematical and numerical tools that are able to predict the crack initiation and propagation and, thus, eliminate their drawbacks.

The underlying research work addresses hydraulic fracture modeling of brittle permeable materials within the energetic phase-field model (PFM) approach. The PFM approximates the sharp edges of the crack by diffusive or smeared-out ones. This is achieved by introducing a scalar-valued phase-field variable to distinguish between the broken and the intact states of the solid material. Moreover, the width of the diffusive edges of the crack is determined through a length scale parameter. With regard to the development of related fracture models and diffusive interface approaches, Griffith [30] discussed the crack surface energy and introduced the definition of the critical energy-release-rate for the brittle fracture onset in elastic solids, which was also supported by experimental results on glass. The Griffith's approach had been substantially extended by Irwin [35], who studied the cracking of ductile materials and discussed the strain-energy release rate and the fracture toughness concept as a new criterion for the initiation of cracks. Apart from fracture mechanics, the approach of diffuse interfaces was used in physics by, e.g. Cahn and Hilliard [13] to describe the interfaces between the different phases of a heterogeneous material by a fourth-order partial differential equation. Later, a link between diffusive interfaces and fracture mechanics was established by Bourdin et al. [9] in an analogy to the work of Mumford and Shah [58] for the modeling of image segmentation problems. Within a variational energy framework of fracture, essential advances were made by, e.g., Francfort and Marigo [27], Bourdin et al. [8], whereas Bourdin et al. [7] extended this to the modeling of hydraulic fracture and compared the crack opening results with the analytical plane strain solutions of Sneddon [69]. A link of variational approach to PFM is found in, e.g., Miehe et al. [52] and Kuhn and Müller [37], which allowed to simulate multi-dimensional, mixed-mode fracture patterns and include dynamic effects and crack branching. To model cracks in anisotropic rocks under a combination of shear and tensile or shear and compressive, Bryant and Sun [11] introduced a mixed-mode I/II phase-field model, whereas the derivations were based on balancing the microforces. Also following the phase-field approach and considering the coupled chemo-hydro-mechanics effects, Choo and Sun [16] treated the cracks in porous materials cased by crystallization of minerals in the pores within a continuum thermodynamical framework. Aldakheel et al. [3] carried out an extension of PFM towards ductile fracture using Gurson-type plasticity at finite strain kinematics. In another work, Aldakheel et al. [2] recently introduced an efficient and new implementation of PFM using the virtual element method (VEM) to model brittle fracture. Within multi-scale modeling, Patil et al. [61] presented a comparative study between the PFM of brittle materials and the physically-motivated molecular dynamics (MD) simulations, which helped to give PFM parameters, like the interface thickness, a physical meaning and realistic estimation. Additional applications and PFM-related solution schemes can also be found in, e.g., Ambati et al. [5], Weinberg and Hesch [74], Cajuhi et al. [14], Miehe et al. [53,51] among others. In connection with hydraulic fracturing of saturated porous materials, permanent changes of the local physics of the material, such as of the volume fractions and the permeability, have to be considered. These effects can be modeled using the PFM together with the macroscopic theory of porous media (TPM) as introduced in Markert and Heider [48,33] and Heider and Markert [25]. A dynamic phase-field brittle fracture model for heterogeneous solids and porous materials with ABAQUS UEL implementation can be found in Pillai et al. [62]. Moreover, a phase-field approach of hydraulic fracturing based on Biot's poroelastic equations was investigated by Mikelić et al. [55,56], Lee et al. [40] and Miehe et al. [54]. In the mentioned works, different features of hydraulic fracture in 2D and 3D settings could be realized and advanced numerical schemes and algorithms were implemented.

A recent extensive literature review of the numerical methods and semi-analytical solutions of hydraulic fracturing can be found in Lecampion et al. [38]. This included the review of the basic hydraulic fracturing models and their extensions, the essential challenges on different scales, as well as a review of advanced numerical schemes. Lecampion et al. [39] carried out comparisons between three laboratory experiments and numerical predictions, where the focus was on hydraulic fracture initiation and propagation in low-permeability materials and constant injection rates. It was shown that the fracture profile is affected by different factors such as the injection rate, fluid viscosity, notch size and injection system compressibility. Further approaches for the modeling of hydraulic fracturing can be found in the literature. The extended finite element method (XFEM) together with the lubrication theory for the fluid flow were implemented by Willbrand et al. [75], Weber and Fries [71] and Weber et al. [72] to model the pressure-induced fracture of linear elastic solid materials. Moreover, a micro-macro-scale approach based on a cohesive-zone model was considered by Réthoré et al. [63,64] and Kraaijeveld and Huyghe [36] to treat the change of the flow type in the cracked region. In Secchi and Schrefler [66], Secchi et al. [67] and [15], the modeling of hydraulic fracturing was carried out using a cohesive, discrete crack model, which required continuous updating of the mesh as the crack tip advances, so that cracks can propagate in arbitrary directions. An approach for the numerical modeling of hydraulic crack propagation and coalescence in brittle rocks, which is based on coupling flow network with discrete element modeling was discussed in Liu et al. [43]. In Li et al. [42], numerical simulation of hydraulic fracturing based on an elastic damage constitutive law with residual strength was applied. To calibrate the numerical model, experimental data of triaxial tests were applied. In Adachi et al. [1], a computer simulation of hydraulic fracturing of hydrocarbon reservoirs, with the fluid flow modeling based on the lubrication theory, was introduced. A Comparison between experimental data and simulations of saucer-shaped hydraulic fractures in impermeable homogeneous elastic solids can be found in Bunger et al. [12]. Detournay [21] introduced a review and analysis of hydraulic fracture-coupled phenomena in permeable and impermeable materials, including far-field stresses, material toughness, and fluid viscosity effect on the evolution of the cracks. In this, a special focus was on the differences in crack propagation behavior between the radial (penny-shaped) and the plane-strain fractures. Based on the PFM and the lubrication theory for the flow in the crack, David et al. [18] introduced a numerical study and analytical validations for the different cases of crack propagation in impermeable and permeable medium. This included the toughness-dominated crack propagation with low-viscous fluids, the viscous-dominated crack propagation with highly-viscous fluids

and the leak-off toughness-dominated case.

For the modeling of the permeable material in this work, the multi-phase continuum-mechanical theory of porous media (TPM) is implemented, see, e.g., de Boer [19], Ehlers [23]. The mathematical description within the TPM results in a set of partial differential equations (PDE). These PDEs belong to the class of strongly-coupled problems, discussed in, e.g., Felippa et al. [26], Matthies et al. [50], Markert [46,47], Obaid et al. [60] and Heider [32]. Thus, for the numerical treatment that includes implicit time integrations and spatial discretization using the finite element method (FEM), special care with regard to the stability should be paid, particularly when the fluid compressibility becomes very low. Moreover, applying the PFM for the hydraulic fracture modeling adds an additional differential equation to the TPM problem. Thus, a suitable time stepping algorithm, consisting of monolithic and staggered solution steps is needed to solve the three-field (elasticity, pressure, phase-field) coupled problem.

The discussed mathematical model is calibrated against laboratory experiments on granite rock samples of the size $30 \times 30 \times 45 \, \text{cm}^3$, i.e. Clauser et al. [17]. For this purpose, 2D and 3D finite element models were constructed, focusing on the comparison with the measured pressure time history as well as the estimated crack radius. It is shown that experimentally-driven pressure curves and fracture topology could be reproduced with a good accuracy by using the proposed TPM-PFM approach.

2. Theoretical fundamentals

2.1. Phase field-extended continuum porous media mechanics

2.1.1. Homogenization, volume fractions and densities

For the mathematical description, the following formulations proceed from a saturated, two-phase porous material consisting of an immiscible and compressible pore-fluid (as a mixture of compressible gas and incompressible liquid) and a compressible solid matrix. The microscopically heterogeneous porous materials can be well described within the macroscopic TPM, where a homogenization process is applied to a representative elementary volume (REV) yielding a smeared-out continuum φ with overlapped, interacting and statistically distributed solid and fluid aggregates φ^α ($\alpha = S$ for solid phase and $\alpha = F$ for pore-fluid phase), see [23]. Having immiscible aggregates, the volume fraction $n^\alpha := \mathrm{d}v^\alpha / \mathrm{d}v$ of φ^α is defined as the ratio of the partial volume element $\mathrm{d}v^\alpha$ to the total volume element $\mathrm{d}v$ of φ. The saturation constraint for a fully saturated medium is then given by

$$\sum_\alpha n^\alpha = n^S + n^F = 1 \quad \text{with} \quad \begin{cases} n^S & : \text{solidity}, \\ n^F & : \text{porosity}. \end{cases} \tag{1}$$

Furthermore, two density functions are defined, namely a material (effective or intrinsic) density $\rho^{\alpha R} := \mathrm{d}m^\alpha / \mathrm{d}v^\alpha$ and a partial density $\rho^\alpha := \mathrm{d}m^\alpha / \mathrm{d}v$, with $\mathrm{d}m^\alpha$ being the local mass element of φ^α. The solid material incompressibility is associated with $\rho^{SR} = \text{const.}$, however, the solid matrix (bulk) is still compressible through the change of n^S. The compressible fluid phase consists of an inseparable mixture of an incompressible liquid phase φ^L and trapped, compressible, ideal gas bubbles φ^G, see [24,22,44,65] for detailed discussions. Within the TPM, a constitutive law for the compressible fluid density is introduced. Here, ρ^{FR} can be expressed in terms of the material densities of the incompressible liquid ($\rho^{LR} = \text{const.}$) and the compressible gas (ρ^{GR}) as

$$\rho^F = n^F \rho^{FR} = n^L \rho^{LR} + n^G \rho^{GR} \quad \text{with} \quad n^F = n^L + n^G. \tag{2}$$

Herein, n^L and n^G are the liquid and gas volume fractions. Assuming that the gas has a barotropic behavior and is governed by the ideal gas law, a constitutive law that relates the effective density ρ^{GR} to the pore-fluid pressure p is provided. Thus, proceeding from an isothermal case and excluding the external influences of p (such as atmospheric pressure [1]), the ideal gas law (see, Holbrow et al. [34]) is given by

$$\rho^{GR} = \frac{M}{R\Theta} p. \tag{3}$$

Herein, R is the universal gas constant, $\Theta = \text{const.}$ is the absolute Kelvin's temperature, and M is the molar mass of the gas. Following this, Eqs. (2) and (3) result in the relation

$$\rho^{FR}(p) = \frac{n^L}{n^F} \rho^{LR} + \frac{n^G}{n^F} \frac{M}{R\Theta} p. \tag{4}$$

2.1.2. Crack in porous media

Continuum porous media theories, such as the TPM or Biot's Theory, require the existence of solid and fluid constituents at each material point of the homogenized domain, thus $0 < \{n^S, n^F\} < 1$. Moreover, the fluid flow is governed by a porous media filter law, such as the Darcy or Forchheimer law, see, e.g. [45]. In the presence of fracture in the porous domain, the crack is considered completely filled with the fluid ($n^F = 1$) and, consequently, $n^S = 0$. Therefore, it is conceivable to treat the fluid flow in the crack following a Stokes-like flow approach, as will be discussed in details in the later sections.

Within the phase-field modeling of fracture, the occurring sharp discontinuity is treated as a diffusive crack and is governed by the

---

[1] In solving initial-boundary-value problems with compressible pore fluid, the external pressure (e.g. atmospheric pressure p_a) is assigned as an initial condition to the problem, so that $\rho^{GR} \neq 0$.

phase-field variable $d^S(\mathbf{x}, t)$ as a function of space $\mathbf{x}$ and time t. In particular, we have

$$d^S(\mathbf{x}, t) \in [0, 1] \quad \text{with} \begin{cases} d^S = 1 & : \text{cracked solid phase,} \\ d^S = 0 & : \text{intact solid phase,} \\ 0 < d^S < 1 & : \text{diffusive interface.} \end{cases} \tag{5}$$

2.1.3. Kinematics of multi-phase continua

Within continuum porous media mechanics, the individual constituents φ^α are considered to have unique states of motion, see, e.g., [10,31]. Thus, having $\mathbf{X}_\alpha$ as the position vector of φ^α in the reference configuration and $\mathbf{x}$ as the position vector in the actual configuration, each constituent has an individual Lagrangian (material) motion function χ_α and has its own velocity field $\mathbf{v}_\alpha$, viz.

$$\mathbf{x} = \chi_\alpha(\mathbf{X}_\alpha, t) \iff \mathbf{X}_\alpha = \chi_\alpha^{-1}(\mathbf{x}, t) \quad \mathbf{v}_\alpha := \acute{\mathbf{x}}_\alpha = \frac{d_\alpha \mathbf{x}}{dt}, \tag{6}$$

with χ_α^{-1} being the inverse (Eulerian or spatial) motion function and

$$(\bullet)'_\alpha := \frac{d_\alpha(\bullet)}{dt} = \frac{\partial(\bullet)}{\partial t} + \text{grad}\,(\bullet) \cdot \mathbf{v}_\alpha \tag{7}$$

representing the material time derivative of an arbitrary vector quantity $(\bullet)$ with respect to the motion of φ^α and $\text{grad}(\bullet) := \partial(\bullet)/\partial \mathbf{x}$. In the underlying study, the solid-phase motion is described using a Lagrangian approach via the solid displacement $\mathbf{u}_S$ and velocity $\mathbf{v}_S$. For the pore-fluid flow, the motion is described either by an Eulerian description using the fluid velocity $\mathbf{v}_F$ or by a modified Eulerian setting via the seepage velocity $\mathbf{w}_F$. In particular, we have

$$\mathbf{u}_S = \mathbf{x} - \mathbf{X}_S, \quad \mathbf{v}_S = (\mathbf{u}_S)'_S, \quad \mathbf{w}_F = \mathbf{v}_F - \mathbf{v}_S. \tag{8}$$

Within a geometric linear framework for the solid deformation, the essential kinematic relation is the linearized small solid strain tensor ε_S, given by

$$\varepsilon_S = \frac{1}{2}(\text{grad}\,\mathbf{u}_S + \text{grad}^T \mathbf{u}_S). \tag{9}$$

Moreover, as no seepage velocity, but only fluid velocity exists in the context of Stokes's flow, $\mathbf{v}_F$ is adopted as the primary unknown for the pore-fluid motion rather than $\mathbf{w}_F$. This coincides with the idea of a unified formulation for the fluid flow in the cracked region and in the surrounding porous domain. In the context of the compressible fluid motion, it is also worth mentioning that the constituents φ^L and φ^G are assumed to have the same states of motion as φ^F and, as a consequence, they have the same velocity and material time derivative, i.e., $\mathbf{v}_L = \mathbf{v}_G \equiv \mathbf{v}_F$ and $(\cdot)'_L = (\cdot)'_G \equiv (\cdot)'_F$, see, e.g., Mahnkopf [44].

2.1.4. Balance relations of porous media

In the following, the assumptions of isothermal and quasi-static states are made in order to simplify the balance relations. Thus, for the resulting purely mechanical model, the governing constituent balance equations with $\alpha = \{S, F\}$ read:

- Partial mass balance:

$$(\rho^\alpha)'_\alpha + \rho^\alpha \text{div}\,\mathbf{v}_\alpha = \hat{\rho}^\alpha. \tag{10}$$

- Partial momentum balance:

$$\mathbf{0} = \text{div}\,\mathbf{T}^\alpha + \rho^\alpha \mathbf{b} + \hat{\mathbf{p}}^\alpha. \tag{11}$$

Herein, $\hat{\rho}^\alpha$ is the mass production or supply term, which fulfills the condition $\hat{\rho}^S + \hat{\rho}^F = 0$ for a closed system with only possible mass supply through the boundary flux. Moreover, the condition $\hat{\rho}^\alpha = 0$ holds true if no mass exchange between the constituents is considered. In dealing with boundary-value problems of hydraulic fracturing, the fluid injection takes place in a certain non-porous part of the domain with $n^F = 1$. To account for this, a local fluid mass supply (or sink) term $\hat{\rho}^F := \hat{\rho}^{Ext}$ will be considered, and $\hat{\rho}^\alpha = 0$ holds except for the location of the source. Thus, a source location function $\mathscr{Q}(\mathbf{x})$ is applied in the fluid mass balance, so that $\mathscr{Q} = 1$ for the source location where the fluid injection takes place and $\mathscr{Q} = 0$ otherwise.

In Eq. (11), $\mathbf{T}^\alpha = (\mathbf{T}^\alpha)^T := \sigma^\alpha$ is the symmetric partial Cauchy stress tensor assuming small strain treatment and non-polar constituents, $\mathbf{b}$ is the mass-specific body force, and $\hat{\mathbf{p}}^\alpha$ is the direct momentum production (local interaction force between φ^S and φ^F). For this, the overall conservation of momentum results in $\hat{\mathbf{p}}^S + \hat{\mathbf{p}}^F = \mathbf{0}$. Eq. (10) with $\alpha = S$, $\hat{\rho}^S = 0$ (no solid mass production), and by application of an analytical integration (see, e.g., [33]), yields the solidity as a secondary variable as

$$(n^S)'_S = -n^S \text{div}\,\mathbf{v}_S \xrightarrow{\text{integration}} n^S = \underbrace{(1-d^S)n_{0S}^S}_{n_d^S} \det\mathbf{F}_S^{-1}, \tag{12}$$

with $\mathbf{F}_S = \partial\mathbf{x}/\partial\mathbf{X}_S$ being the solid deformation gradient and n_{0S}^S is the initial volume fraction of φ^S. The phase-field variable has been

added to Eq. (12)$_2$ in order to make sure that the crack domain is free of the solid phase, i.e., $d^S = 1$ yields $n^S = 0$ and $n^F = 1$. Following this, n^S can further be simplified by mathematical linearization within the small strain approach yielding

$$n^S \approx n_d^S(1-\text{div } \mathbf{u}_S) \quad \text{with} \quad 0 \leqslant n^S < 1. \tag{13}$$

The fluid mass balance results from Eq. (10) with $\alpha = F$ and considering the source term as

$$(\rho^F)'_F + \rho^F \text{div } \mathbf{v}_F = \hat{\rho}^{Ext}\mathscr{Q}(\mathbf{x}). \tag{14}$$

Thus, having $(\rho^F)'_F = (\rho^F)'_S + \text{grad}\rho^F \cdot \mathbf{w}_F$ from the material time derivative in Eq. (7) together with Eq. (12)$_1$ and the saturation condition in Eq. (1) leads to

$$n^F(\rho^{FR})'_S + \rho^{FR}\text{div } \mathbf{v}_S + \text{div } (\rho^{FR}n^F\mathbf{w}_F) = \hat{\rho}^{Ext}\mathscr{Q}(\mathbf{x}). \tag{15}$$

The material time derivative of $\rho^{FR}(p)$, given in Eq. (4), reads

$$(\rho^{FR})'_S = \left[\frac{(\rho^{LR})^2(1 + C)\frac{M}{R\Theta}}{\left(C + \frac{\rho^{LR}}{\rho^{GR}}\right)^2 (\rho^{GR})^2} \right] (p)'_S := \mathscr{K}_F(p)'_S \quad \text{with} \quad C = \frac{n_{0F}^L \rho^{LR}}{n_{0F}^G \rho_{0F}^{GR}}, \tag{16}$$

where n_{0F}^L and n_{0F}^G are the initial volume fractions of φ^L and φ^G, respectively, and ρ_{0F}^{GR} is the initial material gas density, see, e.g. [32] or [44] for more details. In Eq. (16), $\mathscr{K}_F$ controls the compressibility of the fluid in connection with the included volume fraction of the gas constituent.

2.1.5. Effective stresses and permeability formulation

Following the principle of effective stresses, the total stress state at any material point of the homogenized two-phase material consists of an 'extra' or 'effective' stress, indicated by the subscript $(\bullet)_E$, and a weighted pore-fluid pressure term, see [6,20] for a historical review and references. Thus, $\boldsymbol{\sigma}^\alpha$ and $\hat{\mathbf{p}}^\alpha$ with $\alpha = \{S, F\}$ in Eq. (11) can be expressed as

$$\boldsymbol{\sigma}^S = \boldsymbol{\sigma}_E^S - n^S p\mathbf{I}, \quad \boldsymbol{\sigma}^F = \boldsymbol{\sigma}_E^F - n^F p\mathbf{I}, \quad \hat{\mathbf{p}}^F = \hat{\mathbf{p}}_E^F + p\text{grad}n^F. \tag{17}$$

For a linear elastic solid phase, the effective stress tensor $\boldsymbol{\sigma}_E^S$ is derived from the solid free energy function $\Psi_{el}^S(\boldsymbol{\varepsilon}_S)$, as will be discussed in details in Section 2.2. Having the isotropic intrinsic permeability tensor $\mathbf{K}^S = K^S \mathbf{I}$, the constitutive equation of the interaction force $\hat{\mathbf{p}}^F$ can be expressed as

$$\hat{\mathbf{p}}_E^F = -(1-d^S)\frac{(n^F)^2\mu^{FR}}{K^S}\mathbf{w}_F, \tag{18}$$

where $\mu^{FR} > 0$ is the effective fluid viscosity. It follows from Eq. (18) that the interaction force $\hat{\mathbf{p}}_E^F$ decreases gradually as the crack develops ($d^S > 0$), where $\hat{\mathbf{p}}_E^F$ vanishes for a complete crack, filled fully with fluid ($n^F = 1$), see [33]. Alternative to multiplying the interaction term in Eq. (18) by $(1-d^S)$, the degradation of $\hat{\mathbf{p}}_E^F$ in the crack is associated with increase of K^S to a large value that makes $\hat{\mathbf{p}}_E^F$ negligible, which will be discussed in Section 2.1.6. In this contribution, the following relation of the intrinsic permeability K^S in the deformable porous domain is adopted, which considers, the initial permeability K_0^S and the influence of the solid matrix small deformations through $\alpha_\mathbf{u}$:

$$K^S = \alpha_\mathbf{u} K_0^S \quad \text{with} \quad \alpha_\mathbf{u} = \left(\frac{n^F}{n_{0S}^F}\right)^z. \tag{19}$$

In Eq. (19), the parameter $z \geq 0$ influences the deformation-dependency of the permeability, see [45]. Moreover, with the assumptions of a Newtonian fluid and negligible average normal viscous stress (i.e. Stokes's hypothesis), the effective fluid viscous stress can be expressed as

$$\boldsymbol{\sigma}_E^F = \mu^F(\text{grad}\mathbf{v}_F + \text{grad}^T \mathbf{v}_F), \tag{20}$$

with $\mu^F := n^F\mu^{FR} > 0$ being the partial shear or dynamic viscosity.

2.1.6. Fluid flow in the crack and the surrounding porous domain

Eq. (11) together with (18) and (20) yield the fluid momentum balance, which describes after putting $d^S = 0$ the fluid flow in the non-crack porous region. In particular, it reads

$$\mathbf{0} = \mu^{FR}\text{div } \text{grad}(\mathbf{v}_F) - n^F\text{grad}p + \rho^F\mathbf{b} - (1-d^S)\frac{(n^F)^2\mu^{FR}}{K^S}(\mathbf{v}_F - \mathbf{v}_S). \tag{21}$$

On the other hand, the fluid flow within the fracture domain with crack width w_c is assumed to be similar to the laminar flow of a Newtonian viscous fluid between two parallel plates with a distance w_c as illustrated in Fig. 1, see, e.g., [70].

The fluid momentum balance Eq. (21) with ($d^S = 1$) for the crack region yields Stokes free flow equation:

$$\mathbf{0} = \mu^{FR}\text{div } \text{grad}(\mathbf{v}_F) - \text{grad}p + \rho^{FR}\mathbf{b}. \tag{22}$$
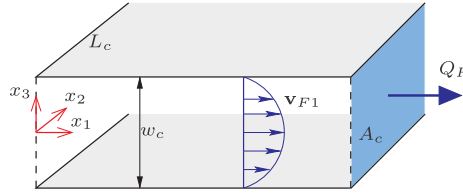
Fig. 1. Schematic illustration of the crack opening with width w_c and depth L_c in x_2 direction, where $v_{F1}(x_3 \pm w_c/2) \approx 0$.

This equation can further be reformulated considering the geometry of the crack, which results in a modified Darcy's law for the flow in the crack region. Thus, integration of Eq. (22) in x_1-direction and considering the related boundary conditions yields the volume flux per unit area of the crack cross section q_{F1} as

$$q_{F1} = Q_F/A_c = -\frac{w_c^2}{12\mu^{FR}}\left[\frac{\partial p}{\partial x_1} - \rho^{FR}b_1\right]. \tag{23}$$

For a general crack orientation, Eq. (23) can be rewritten in a vector form as

$$\mathbf{q}_F = -\frac{w_c^2}{12\mu^{FR}}[\mathrm{grad}\,p - \rho^{FR}\mathbf{b}]. \tag{24}$$

Eq. (24) governs the fluid flow in the crack and has a structure similar to that of Darcy's law in porous media. Therefore, it can be rewritten as

$$\mathbf{v}_F = \mathbf{q}_F = -\frac{K_c}{\mu^{FR}}[\mathrm{grad}\,p - \rho^{FR}\mathbf{b}] \quad \text{with} \quad K_c := \frac{w_c^2}{12} \tag{25}$$

representing the permeability in the crack. In the underlying work, a linear relation that considers the gradual change of the permeability between the crack (K_c, $d^S = 1$) and the surrounding porous medium (K_0^S, $d^S = 0$) is proposed;

$$K^S = \alpha_\mathbf{u} K_0^S + d^S(K_c - \alpha_\mathbf{u} K_0^S). \tag{26}$$

With regard to the crack width, if the crack path is predictable, then an average value of w_c can directly be estimated based on the current values of the displacements at the crack edges. Alternatively, w_c can be approximated at each quadrature point using the normal vector of the crack boundary $\mathbf{n}_c = \frac{\mathrm{grad}\,d^S}{\|\mathrm{grad}\,d^S\|} = n_{ci}\mathbf{e}_i$, the finite element length at crack path h_e and the components ε_{ii} of the strain tensor ε_S. For instance, the crack width in the 2D settings reads

$$w_c := \sqrt{[h_e(1 + \varepsilon_{11})n_{c1}]^2 + [h_e(1 + \varepsilon_{22})n_{c2}]^2}, \tag{27}$$

see, e.g. [59,76] for more details about the smeared displacement jump approximation. As an alternative to the above, accurate level-set approaches for computation of the fracture opening and a subsequent finite element interpolation of the width were introduced in [41].

2.2. Energy-based PFM formulation

According to the description of brittle fracture introduced by [30], the overall potential energy $\mathscr{F}$ of a cracked linear elastic and isotropic solid can be given as the sum of the elastic strain energy $\overline{\Psi}_{\mathrm{el}}^S$, integrated over the whole spatial domain Ω, and the critical fracture energy G_c, required to create a unit area of the fracture surface, integrated along the crack path Γ_c. Thus,

$$\mathscr{F}(\varepsilon_S, \Gamma_c) = \int_\Omega \overline{\Psi}_{\mathrm{el}}^S(\varepsilon_S)\,\mathrm{d}v + \int_{\Gamma_c} G_c\,\mathrm{d}\Gamma_c. \tag{28}$$

For the aim of an easier numerical implementation in standard finite element packages, the PFM has been incorporated in the energetic fracture approach, where a phase-field variable d^S is introduced to approximate the sharp crack edges by diffusive transition zones. Following this, the potential energy function in Eq. (28) is rewritten as an integration over the whole body:

$$\mathscr{F}(\varepsilon_S, d^S, \nabla d^S) = \int_\Omega [\Psi_{\mathrm{el}}^S(\varepsilon_S, d^S) + \Psi_{\mathrm{crack}}^S(d^S, \nabla d^S)]\,\mathrm{d}v. \tag{29}$$

The onset of fracture is associated with a degradation of the solid elastic energy, which is assumed in this work to occur under tension and shear and not under compression. Thus, the elastic energy is split into a positive part Ψ_{el}^{S+}, including the tensile and the shear response, and a negative part Ψ_{el}^{S-} that includes the compressive response. Moreover, the degradation of Ψ_{el}^{S+} is realized through the degradation function $\mathscr{G}_d := [(1-\eta)(1-d^S)^2 + \eta]$ with $0 < \eta \ll 1$ being a small residual stiffness parameter needed to ensure the numerical stability by preventing zero stiffness in the momentum balance (see, e.g., [37,55]). However, η is set equal to zero in the phase-field evolution equation as here no stability-related challenges exist. In particular,

$$\Psi_{el}^S(\varepsilon_S, d^S) = \mathscr{G}_d \Psi_{el}^{S+} + \Psi_{el}^{S-} =$$
$$\mathscr{G}_d \left[\frac{1}{2}\kappa^S [tr^+(\varepsilon_S)]^2 + \mu^S \varepsilon_S^D \cdot \varepsilon_S^D \right] + \frac{1}{2}\kappa^S [tr^-(\varepsilon_S)]^2 \tag{30}$$

with $\kappa^S := \lambda^S + \frac{2}{3}\mu^S$ being the bulk modulus of the porous solid matrix, given in terms of the macroscopic Lamé constants μ^S and λ^S. Moreover, $tr(\varepsilon_S) := \varepsilon_S \cdot \mathbf{I} = \text{div } \mathbf{u}_S$ is the scalar-valued trace of the strain tensor ε_S and $\varepsilon_S^D := \varepsilon_S - \frac{1}{3}tr(\varepsilon_S)\mathbf{I}$ is its deviator. The positive and negative traces of the strain tensor are simply defined as $tr^+(\varepsilon_S) = \max\{0, tr(\varepsilon_S)\}$ and $tr^-(\varepsilon_S) = \min\{0, tr(\varepsilon_S)\}$, respectively. Following this, the effective solid stress tensor is defined as

$$\sigma_E^S = \frac{\partial \Psi_{el}^S(\varepsilon_S, d^S)}{\partial \varepsilon_S} = \mathscr{G}_d [\kappa^S tr^+(\varepsilon_S)\mathbf{I} + 2\mu^S \varepsilon_S^D] + \kappa^S tr^-(\varepsilon_S)\mathbf{I}. \tag{31}$$

The fracture energy as a function of d^S and its gradient ∇d^S can be expressed according to [52] as

$$\Psi_{crack}^S(d^S, \nabla d^S) = G_c \gamma_d(d^S, \nabla d^S) = \frac{G_c}{2 \epsilon}[(d^S)^2 + \epsilon^2 |\nabla d^S|^2] \tag{32}$$

with $\gamma_d(d^S, \nabla d^S)$ representing the crack density function per unit volume and ϵ is a regularization parameter (internal length) that controls the width of the transition zone between the cracked and the intact zones.

Having $\Psi := \Psi_{el}^S + \Psi_{crack}^S$, a phase-field evolution relation is derived following the Allen–Cahn approach ([4]), which uses a reaction-diffusion equation to express the process of phase separation like crack formation:

$$\frac{d d^S(\mathbf{x}, t)}{dt} = (d^S)_S' = -M\frac{\partial \Psi}{\partial d^S}$$
$$= -M\left[-2(1-d^S)\Psi_{el}^{S+} + G_c\frac{\partial \gamma_d}{\partial d^S}\right]$$
$$= -M\left[-2(1-d^S)\Psi_{el}^{S+} + \frac{G_c}{\epsilon}(d^S - \epsilon^2 \Delta d^S)\right]. \tag{33}$$

Herein, $M > 0$ is a scalar-valued interface mobility parameter controlling the time scale of the phase-field evolution. Adopting a constant value of M yields a conventional Ginzburg–Landau evolution equation, see, e.g., [37,54,57]. Additionally, $\Delta(\bullet) := \text{div grad}(\bullet)$ denotes the Laplace operator. For rate-independent settings with $1/M (d^S)_S' \approx 0$, Eq. (33) is reformulated according to [54] yielding

$$\underbrace{(1-d^S)\overline{\mathscr{D}_c}}_{\text{driving force}} = \underbrace{[d^S - \epsilon^2 \Delta d^S]}_{\text{geometric resistance}}, \tag{34}$$

where

$$\overline{\mathscr{D}_c} := \frac{2\Psi_{el,max}^{S+}}{G_c/\epsilon} \quad \text{and} \quad \Psi_{el,max}^{S+} := \max_{\tau \in [0,t]} \Psi_{el}^{S+}(\varepsilon_S(\mathbf{x}, \tau)). \tag{35}$$

Herein, $\Psi_{el,max}^{S+}$ represents the maximum positive elastic strain energy density, which is introduced following [52] to prevent crack healing and to assure the irreversibility of the phase-field variable during cyclic loading.

The formulations (34) and (35) are thermodynamically consistent and widely used in phase-field modeling of fracture. However, as the crack driving force $\overline{\mathscr{D}_c}$ is proportional to $\Psi_{el,max}^{S+}(\varepsilon_S)$, it increases once the material is under tension or shear, leading to degradation of the solid stiffness at lower values of the stresses. To avoid this undesired effect, Miehe et al. [54] suggested a modified crack driving criterion that enforces the crack driving force to be zero as long as the occurring elastic strain energy or the stresses remain below a certain threshold. These extensions of the PFM are based on formulations introduced within gradient-damage mechanics as, e.g., in [29,28]. Thus, introducing ψ_c as a specific fracture energy per unit volume and modifying the crack energy formulation according to [54], the fracture energy Eq. (32) becomes

$$\widetilde{\Psi}_{crack}^S(d^S, \nabla d^S) = 2\psi_c\left[(d^S) + \frac{\epsilon^2}{2}|\nabla d^S|^2\right], \tag{36}$$

and the total energy after some algebraic reformulation reads

$$\widetilde{\Psi} = \Psi_{el}^S + \widetilde{\Psi}_{crack}^S = (1-d^S)^2[\Psi_{el}^{S+} - \psi_c] + \psi_c + \Psi_{el}^{S-} + 2\psi_c \epsilon \gamma_d(d^S, \nabla d^S). \tag{37}$$

Applying $\partial \widetilde{\Psi}/\partial d^S = 0$ yields a modified driving force $\widetilde{\mathscr{D}_c}$ in Eq. (34), which is independent of the internal length scale ϵ and expressed as

$$\widetilde{\mathscr{D}_c} = \max_{\tau \in [0,t]} \left\langle \frac{\Psi_{el}^{S+}(\varepsilon_S)}{\psi_c} - 1 \right\rangle_+. \tag{38}$$

In this, $\langle (\bullet) \rangle_+ = \frac{1}{2}[(\bullet) + |(\bullet)|]$ represents the Macauley brackets. On the one hand, this formulation enforces the crack driving force to be equal to zero as long as $\Psi_{el}^{S+} < \psi_c$. On the other hand, it prevents crack healing as $\widetilde{\mathscr{D}_c}$ always increases. In case of hydraulic fracturing, the fluid pressure accumulation is the cause for the onset and propagation of the fracture. This can be well explained based on the effective stress relations (17)$_{1,2}$ for a biphasic porous material, which can be rewritten as

$$\boldsymbol{\sigma} := \boldsymbol{\sigma}^S + \boldsymbol{\sigma}^F \approx \boldsymbol{\sigma}_E^S - p\mathbf{I}, \tag{39}$$

where $\boldsymbol{\sigma}$ represents the total stress. Following this, Eq. (39) can further be reformulated by including the definitions of the mean total stress $\sigma_m := \frac{1}{3}\mathrm{tr}(\boldsymbol{\sigma})$ and the mean effective stress $\sigma_{E,m}^S := \frac{1}{3}\mathrm{tr}(\boldsymbol{\sigma}_E^S)$ as scalar quantities yielding

$$\sigma_m = \sigma_{E,m}^S - p \quad \text{with} \quad \sigma_{E,m}^S = \sigma_{E,m}^{S+} + \sigma_{E,m}^{S-}, \tag{40}$$

where $\sigma_{E,m}^{S+} := \max\{0, \sigma_{E,m}^S\}$ and $\sigma_{E,m}^{S-} := \min\{0, \sigma_{E,m}^S\}$. During pore-pressure increase, $\sigma_{E,m}^S$ changes from a state of compression, i.e. $\sigma_{E,m}^{S-} \neq 0$ and $\sigma_{E,m}^{S+} = 0$, to a state of tension, i.e. $\sigma_{E,m}^{S+} \neq 0$ and $\sigma_{E,m}^{S-} = 0$, where the crack onset corresponds to a critical fracture mean stress. In 1D settings, a critical tensile stress σ_{crit}^S for the fracture initiation is provided, which can also be determined by relatively simple experiments. In this, the cracking starts when the tensile stress (equal to the positive principal effective stress $\sigma_{E,p}^{S+}$) exceeds the value of σ_{crit}^S. Therefore, the energy formulations that enter Eq. (38) in case of linear elasticity read

$$\Psi_{\mathrm{el}}^{S+} = \frac{1}{2E^S}(\sigma_{E,p}^{S+})^2, \qquad \psi_c = \frac{1}{2E^S}(\sigma_{crit}^S)^2 \tag{41}$$

with E^S being Young's modulus. Following this for multi-dimensional, isotropic linear elastic settings, as given in [54], the following simplified crack driving function is introduced:

$$\widetilde{\mathscr{D}_c} = \max_{\tau \in [0,t]} \left\langle \sum_{i=1}^{3} \left(\frac{\sigma_{E,pi}^{S+}}{\sigma_{crit}^S} \right)^2 - 1 \right\rangle_+ , \tag{42}$$

which is implemented in the numerical examples of this work. In this, $\sigma_{E,pi}^{S+}$ with $i \in \{1, 2, 3\}$ are the principal stresses in the three principal directions.

2.3. Governing balance equations (up-d formulations)

The balance Eqs. (10) and (11) together with the kinematic and constitutive relations in the previous sub-sections result in the governing partial differential equations (PDE) with primary unknowns $\{\mathbf{u}_S, \ p, \ d^S\}$. In this, the assumption of negligible fluid shear stress $\boldsymbol{\sigma}_E^F$ in the intact porous domain to reduce the number of primary variables by eliminating $\mathbf{v}_F$ has been applied. Moreover, the fluid momentum balance has been used to reformulate the fluid mass balance in order to eliminate the fluid velocity term. Noting that this reformulation improves also the numerical stability, especially for the case of very low fluid compressibility, where the structure of the system of equations becomes similar to that of differential-algebraic equations (DAE) with differential index higher than one (see [49]). In summary, the *up-d* formulations read.

- Overall momentum balance:

$$\mathbf{0} = \mathrm{div}\ \underbrace{[\boldsymbol{\sigma}_E^S(\mathbf{u}_S, d^S) - p\mathbf{I}]}_{\boldsymbol{\sigma}} + \rho\mathbf{b}. \tag{43}$$

- Fluid mass balance:

$$n^F \mathscr{K}_F (p)_S' + (1 - d^S)\rho^{FR}\mathrm{div}\ \mathbf{v}_S$$
$$- \ \mathrm{div}\left[\rho^{FR}\frac{K^S}{\mu^{FR}}(\mathrm{grad}p - \rho^{FR}\mathbf{b})\right] = \hat{\rho}^F. \tag{44}$$

- Phase-field evolution equation:

$$0 = (1 - d^S)\widetilde{\mathscr{D}_c} - [d^S - \epsilon^2\ \Delta d^S]. \tag{45}$$

3. FE implementation

The finite element method (FEM) is applied for the numerical solution of initial-boundary value problems (IBVP) of hydraulic fracturing. In the FEM, Eqs. (43)–(45) with primary variables $\{\mathbf{u}_S, \ p, \ d^S\}$ are weighted by independent test functions $\{\delta\mathbf{u}_S, \ \delta p, \ \delta d^S\}$ and integrated over the spatial domain Ω to derive the weak formulation. Moreover, the product rule and the Gaussian integral theorem are applied to get the boundary terms $\Gamma = \partial\Omega$, where Γ is split into Dirichlet (essential) and Neumann (natural) boundaries (for a detailed discussion, see, e.g., [32,49,77] among many others). Following this, the overall aggregate momentum balance in a weak form reads

$$\int_{\Omega} \mathrm{grad}\delta\mathbf{u}_S \cdot \boldsymbol{\sigma}\,\mathrm{d}v - \int_{\Gamma_t} \delta\mathbf{u}_S \cdot \bar{\mathbf{t}}\,\mathrm{d}a - \int_{\Omega} \delta\mathbf{u}_S \cdot \rho\mathbf{b}\,\mathrm{d}v = 0 \tag{46}$$

with $\bar{\mathbf{t}} = \boldsymbol{\sigma}\mathbf{n}$ being the external traction vector acting on the Neumann boundary Γ_t of the overall aggregate with outward-oriented unit surface normal $\mathbf{n}$. The fluid mass balance in weak form reads

$$\int_\Omega \delta p (n^F \mathscr{K}_F)(p)'_S \mathrm{d}v + \int_\Omega \delta p (1-d^S)\rho^{FR} \mathrm{div}\ \mathbf{v}_S \mathrm{d}v +$$

$$\int_\Omega \mathrm{grad}\delta p \cdot \rho^{FR} \frac{K^S}{\mu^{FR}} (\mathrm{grad}p - \rho^{FR}\mathbf{b})\mathrm{d}v + \int_{\Gamma_v} \delta p \bar{v} \mathrm{d}a = \int_\Omega \delta p (\hat{\rho}^F)\mathrm{d}v \tag{47}$$

with $\bar{v} = n^F \mathbf{w}_F \cdot \mathbf{n}$ denoting the volume efflux of the fluid draining through the Neumann boundary Γ_v. For a cracked medium, this boundary term becomes $\bar{v} \approx \mathbf{v}_F \cdot \mathbf{n}$. The weak formulation of the phase-field evolution Eq. (45) can be expressed as

$$\int_\Omega \delta d^S [(1-d^S)\widetilde{\mathscr{D}_c} - d^S]\mathrm{d}v - \int_\Omega \mathrm{grad}\delta d^S \cdot (\epsilon^2\ \mathrm{grad}d^S)\mathrm{d}v + \int_{\Gamma_d} \delta d^S\ \epsilon^2(\mathrm{grad}d^S \cdot \mathbf{n})\mathrm{d}a = 0, \tag{48}$$

where Γ_d corresponds to a Neumann boundary. It is worth mentioning that in the numerical examples, $\mathrm{grad}d^S \cdot \mathbf{n} = 0$ has been adopted, such that the boundary integral in Eq. (48) vanishes.

For the spatial semi-discretization and the finite element treatment, the procedure of Bubnov-Galerkin is applied to Eqs. (46)–(48). The primary variables are collected in the vector $\mathbf{u} := [\mathbf{u}_S\ p\ d^S]^T$, whereas their time-dependent nodal coefficients are expressed as $\mathbf{u}_{(i)} := [\mathbf{u}_S\ \mathbf{p}\ \mathbf{d}^S]^T$. Distinguishing between the TPM and the PFM problem yields the following coupled, space-discrete PDE system, written in an abstract form as

$$\begin{bmatrix} \mathcal{G}^h_{TPM}(t, \mathbf{y}, (\mathbf{y})'_S; \mathbf{d}^S) \\ \mathcal{G}^h_{PFM}(t, \mathbf{d}^S, (\mathbf{d}^S)'_S; \mathbf{y}) \end{bmatrix} \overset{!}{=} \mathbf{0} \tag{49}$$

with $\mathbf{y} := \mathbf{y}(t) = [\mathbf{u}_S\ \mathbf{p}]^T$. In Eq. (49), $\mathcal{G}^h_{TPM}$ represents the space-discrete, strongly coupled TPM problem, which results from Eqs. (46) and (47), whereas $\mathcal{G}^h_{PFM}$ is the space-discrete phase-field evolution equation resulting from Eq. (48).

The time integration is carried out using a staggered procedure between $\mathcal{G}^h_{TPM}$ and $\mathcal{G}^h_{PFM}$, whereas the couple equations in $\mathcal{G}^h_{TPM}$ are solved using a monolithic implicit approach. In particular, the implicit 2nd-order backward difference formula (BDF2) scheme, that gives a good trade-off between stability, accuracy and computational costs, is used for the time discretization. To calculate the solution at time $t_{(k+1)} = t_{(k)} + \Delta t$ with Δt being the time increment, and having the values of the variables $\{\mathbf{u}_S\ \mathbf{p}\ \mathbf{d}^S\}$ from the last two time steps $t_{(k)}$ and $t_{(k-1)}$, the applied procedure is summarized in the following steps:

i. Calculation of the crack deriving force $\widetilde{\mathscr{D}_c}$ based on the data from $t_{(k)}$.
ii. Solving $\mathcal{G}^h_{PFM}$ using the BDF2 and $\widetilde{\mathscr{D}_c}$ from step (i)
    $\longrightarrow\quad \mathbf{d}^S_{(k+1)}$.
iii. Monolithic solution of $\mathcal{G}^h_{TPM}$ using the BDF2 and $\mathbf{d}^S_{(k+1)}$
    $\longrightarrow\quad \mathbf{u}_{S(k+1)}, \mathbf{p}_{(k+1)}$.
iv. Check the error limit and update the time step.

In this procedure, time adaptivity is applied to keep the temporal error below a certain limit. More information and references to the solution of coupled problems can be found in, e.g, [46,47,49,60].

3.1. Crack opening displacement under static pressure

As a first verification of the model, we compare the analytical solution of crack opening displacement under static pressure in an infinite domain from the literature with numerical solutions of the underlying model, see [69,7,18] for references. The chosen material properties of the homogeneous and elastic domain are, as given in [18], the Young's modulus $E = 17$ GPa, the Poisson's ratio $\nu = 0.2$, whereas the net pressure in the crack $p_f = 2.25 \times 10^5$ Pa and the total crack length $2L_f = 4$ m (Fig. 2, left). The analytical solution of the fracture displacement (Sneddon [69]) is expressed by
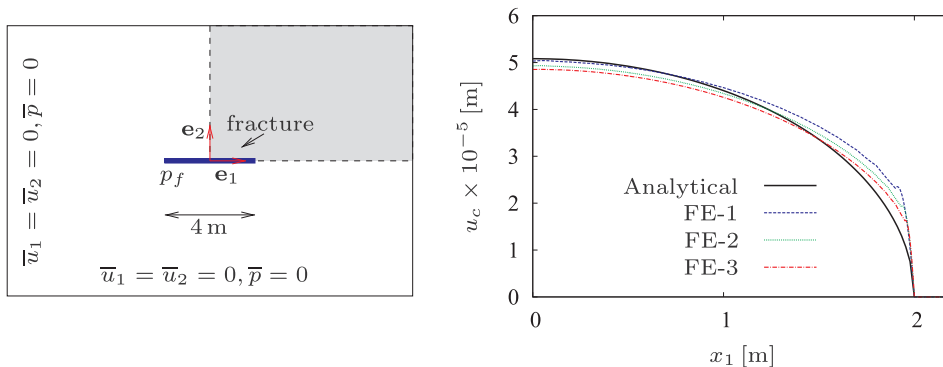
Fig. 2. Geometry (double symmetry) with dimensions (90 m×60 m) and boundary conditions of the crack opening problem (left). Fracture opening profile (right) for the analytical and the numerical solutions with different mesh sizes (h_e) and length scales (l_c) as FE-1 with $h_e = 0.1$ m, $l_c = 0.2$ m, FE-2 with $h_e = 0.07$ m, $l_c = 0.14$ m and FE-3 with $h_e = 0.05$ m, $l_c = 0.1$ m.

Table 1
Parameters of the granite rock samples and the injected fluid.

Parameter	Sym.	Val.	Unit
Young's modulus of φ^S	E^S	$36.9 \cdot 10^9$	Pa
Possion's ratio of φ^S	ν^S	0.3	–
Tensile strength	σ_t^S	$13.5 \cdot 10^6$	Pa
Initial intrinsic permeability	K_{0S}^S	$5 \cdot 10^{-19}$	m^2
Effective solid density	ρ^{SR}	2670	kg/m^3
Initial solidity	n_{0S}^S	0.99	–
Effective liquid density	ρ^{LR}	1575	kg/m^3
Initial density of ideal gas	ρ_{0S}^{GR}	1.25	kg/m^3
Eff. dyn. fluid viscosity	μ^{FR}	1.48	N s/m^2
Initial volume fraction of gas*	n_{0S}^G	0.009	–
Universal gas constant	R	8.3144	J/K mol
Absolute Kelvin's temperature	Θ	273.15	K
Molecular mass of dry air	M	2.897	kg/mol

* This initial gas fraction corresponds to dry rock with 90% air in the pores.

$$u_c(\mathbf{x}) = \frac{2p_f L_f}{E'} \sqrt{1 - \left(\frac{\mathbf{x}}{L_f}\right)^2} \quad \text{with} \quad E' := \frac{E}{1-\nu^2}.$$
(50)

In the numerical simulation, the aforementioned material properties have been assigned to the solid phase, whereas the effect of the fluid in the domain has been eliminated by choosing very high compressibility ($\mathscr{K}_F = 1\frac{Pa\,kg}{m^3}$). The other material parameters can be found in Table 1. Due to the double symmetry (Fig. 2, left), only quarter of the domain has been modeled, where different mesh sizes and internal length scales have been tested. At the crack boundary, the phase-field variable was set to 1 ($d^S = 1$) and the pressure $p = p_f$, representing a Dirichlet boundary condition of the fluid mass balance in Eq. (44). Fig. 2, right, shows a good approximation of the crack opening displacement using the considered model, especially when using fine mesh and a small value of the length-scale parameter.

4. Laboratory experiments

Reproducible and well-constrained laboratory experiments on hydraulic fracture propagation through crystalline rock samples were conducted as part of a joint project between 2010 and 2015 at the Chair of Geotechnical Engineering, RWTH Aachen University, see [17]. Below, we briefly describe the setup and execution of these experiments. For a more comprehensive description, the reader is also referred to [68].

4.1. Experimental setup

Hydraulic fracture experiments were conducted on cuboid, $300 \times 300 \times 450$ mm^3 sized granite samples, retrieved from the quarry "Höhenberg", located in easternmost Bavaria, Germany. A list of physical rock properties is provided in the final report of the joint project [17]. A borehole with a radius of 10 mm was centrally drilled through each granite sample with the borehole being oriented parallel to the long axis of the sample. In order to control the location of fracture initiation, a notch, transversely oriented to the borehole and radially penetrating the borehole by 7 ± 1 mm, was induced into each rock sample.

In the hydraulic injection system (illustrated in Fig. 3), fluid was injected using a high-pressure syringe pump (Teledyne Isco 260 HP), connected via stainless steel pipes to the fluid source as well as to the injection interval. A packer, used for isolating the injection interval from the remaining parts of the borehole, represents an in-house construction, consisting of an aluminum core sandwiched between two sealing rings, which were squeezed against the borehole wall by tightening two outer threaded washers. The total fluid volume that can enter the injection system, excluding the volume in the pump, is estimated at 12 cm^3. The fluid pressure was monitored with an accuracy of 0.1 MPa at two pressure transducers, connected to the inlet (P_1) and outlet (P_2) of the injection interval, positioned equidistantly away from the packer. The fluid pressure, calculated as the mean value from both pressure transducers, represents an important experimental quantity that is directly compared to the simulated pressure curves in this study. For generating a slowly propagating fracture that does not reach towards the edges of the sample, glycerol with a dynamic viscosity of ca. 1.4 Pa s turned out to be a suitable injection fluid. In order to trace the fluid pathways after each experiment on split samples, two weight percent of ink were added to the glycerol, see [68]. Prior to fluid injection, each sample was placed into a triaxial testing facility, illustrated in Fig. 4. Flat jacks supplied a pre-defined vertical (5 MPa) and horizontal (15 MPa) stress to the sample, stabilized by three monolithic steel frames as horizontal counter bearings and four column frame as vertical counter bearings. In order to keep the principal stresses applied to the sample constant throughout the experiment, the pressure was monitored at each pair of flat jacks and, if necessary, adjusted automatically by a computer-controlled three pumping units, one for each stress direction.
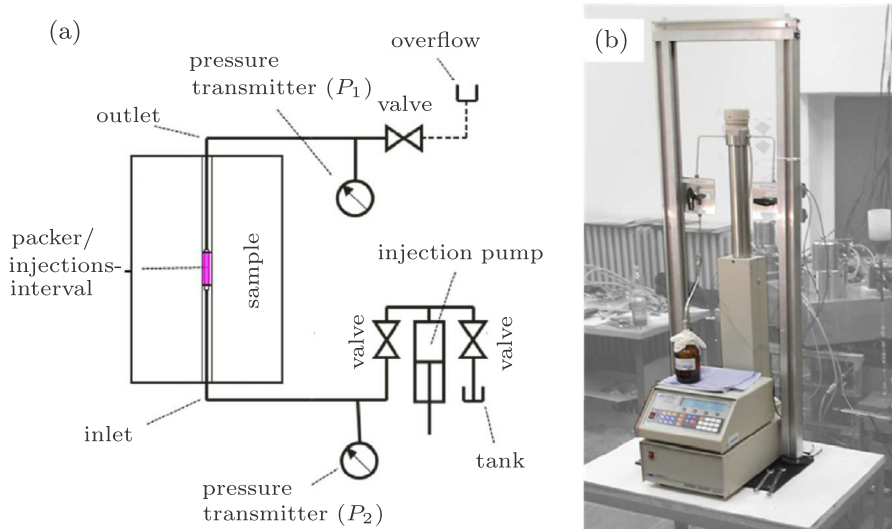
Fig. 3. (a) Schematic illustration of the hydraulic injection system. (b) Picture of the high-pressure syringe injection pump [17].
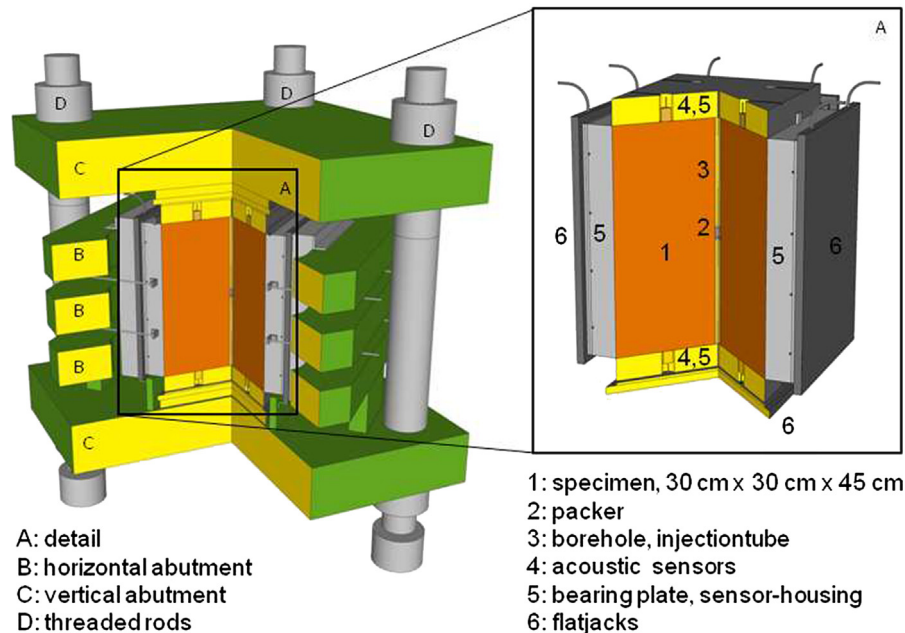

1: specimen, 30 cm × 30 cm × 45 cm
2: packer
3: borehole, injectiontube
4: acoustic sensors
5: bearing plate, sensor-housing
6: flatjacks

A: detail
B: horizontal abutment
C: vertical abutment
D: threaded rods

Fig. 4. Illustration of the triaxial testing facility of hydraulic fracture experiments, see [72]2.

4.2. Experiment execution

In order to achieve the maximum control on fracture propagation after fracture initiation, a two-step injection cycle was carried out (see Fig. 5 as an example). The first injection cycle (*cycle 1*) was run by applying a pumping rate of $q_F = 1.0 \, \text{cm}^3/\text{min}$ until a fluid pressure of $p = 0.5$ MPa was reached. Then, the pumping rate was reduced to $q_F = 0.1 \, \text{cm}^3/\text{min}$. When reaching the peak pressure (crack initiation), the pressure valve next to the injection interval was opened for immediate pressure release and termination of fracture onset. This cycle helped in eliminating the remaining air in the injection system and in the notch, whereby, due to the high viscous dissipation, no crack propagation took place. Subsequently, the pump cylinder volume was set to its initial value (5 cm³) and after a break of 1800 s, the second injection cycle (*cycle 2*) was run, representing the actual fracking experiment. During this cycle, a pumping rate of $q_F = 1.0 \, \text{cm}^3/\text{min}$ was applied until reaching a fluid pressure of 4 MPa. Then, the pumping rate was reduced to $q_F = 0.1 \, \text{cm}^3$ and then to $q_F = 0.05 \, \text{cm}^3/\text{min}$. Once a peak pressure was reached, injection continued for a pre-defined time, 1800 s in case (1) and 85 s in case (2), before the injection was stopped. Each experimental setup, i.e. cases (1) and (2), has been repeated three times in order to ensure reproducibility of the hydraulic fracture experiment. After each experiment, the fractured sample was split
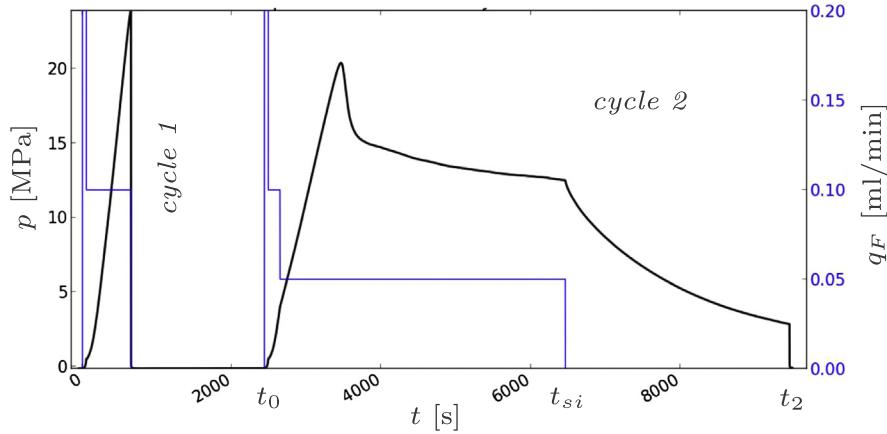
Fig. 5. Exemplary pressure and injection time histories during the experiment ([17]).

parallel to the fracture surface. Fracture surfaces were visually identified by tracing the extent of the colored injection fluid across the cutted sample (Fig. 6).

The fracture radius was defined as the radius of a best fit circle and represents the second important experimentally-derived quantity that we use for comparison with the simulation results in this study.

4.3. Modification of fluid mass balance

The experiments showed that the system, consisting of the pump, the pipes, the packer and the sample, expanded due to increase of the fluid pressure prior to crack initiation, and then contracted elastically during crack propagation associated with a drop of the fluid pressure. This system compressibility, which is also affected by the used fluid viscosity, has a major influence on the crack propagation and the related pressure time history. For the sake of model calibration with the experimental results, the influence of system compressibility on the pressure time history has to be taken into account. This effect can be described by a proportionality between the injection rate at the injection pump (ΔQ) and the pore-pressure increase (Δp) as $\Delta Q \propto \mathscr{K}_{sys}(p)'_S$, see [73,39]. Moreover, it has been noticed in the experiments that the system compressibility starts to decrease by increasing the fluid pressure p, see [68]. Thus, a relation for the system compressibility (total injection system compliance) $\mathscr{K}_{sys}(\overline{\mathscr{K}_{sys}}, p)$ as a function of p and the initial value of the system compressibility $\overline{\mathscr{K}_{sys}}$ should be provided. In the fluid mass balance (44), the fluid compressibility term $\mathscr{K}_F$ depends mainly on the volume fraction of the gas n^G in the fluid. This is not sufficient to capture the measured behavior of the fluid pressure in the injection system, where the system compressibility dominates over the fluid compressibility. For this reason, a total compressibility factor, i.e. $\mathscr{K}_t = f(\overline{\mathscr{K}_{sys}}, p, \mathscr{K}_F)$ should be considered instead of merely $\mathscr{K}_F$. In particular, an empirical relation of the total compressibility is suggested:

$$\mathscr{K}_t = (1/p_e \overline{\mathscr{K}_{sys}} + n^F \mathscr{K}_F) \quad \text{with} \quad p_e = \begin{cases} 1 & \text{if } p \leqslant p_c, \\ p & \text{otherwise.} \end{cases} \tag{51}$$

In this, p_e is a pressure threshold, above which the total compressibility starts to decrease. Noting that the entries of $\mathscr{K}_t$ are determined based on the comparison of the pressure-time record slope between the model and the experiment. Following this, the modified fluid mass balance reads

$$\mathscr{K}_t(p)'_S + (1-d^S)\rho^{FR}\text{div } \mathbf{v}_S$$
$$- \text{div}\left[\rho^{FR}\frac{K^S}{\mu^{FR}}(\text{grad}p - \rho^{FR}\mathbf{b})\right] = \hat{\rho}^{Ext}\mathscr{Q}(\mathbf{x}), \tag{52}$$

Fig. 6. Split sample after finishing the experiment to measure the crack radius ([17]).
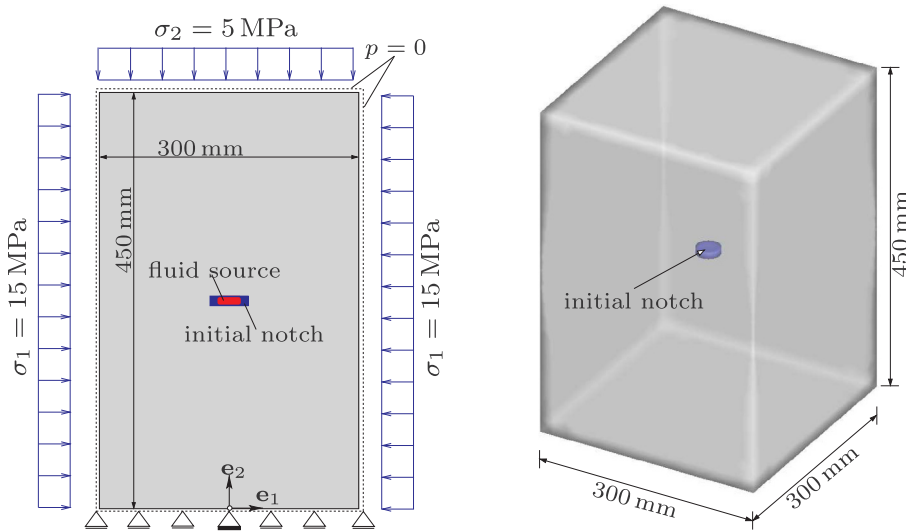
Fig. 7. Geometry and boundary conditions of the 2D and 3D numerical models. The notch in the 2D model is a rectangle with dimensions 36 mm × 7 mm, and in the 3D model is a cylinder of diameter 36 mm and a hight 10 mm.

which will be used in the following examples.

5. Numerical simulation and calibration using experimental data

The following section presents 2D and 3D finite element solutions of the discussed TPM-PFM approach of hydraulic fracturing using the FE package FlexPDE (professional version 6.4, Linux86 64). The material parameters of the granite rock samples together with the fracturing fluid properties, based mainly on experimental investigations [17], are summarized in Table 1.

The geometry and the boundary conditions of the initial-boundary-value problems (IBVP) are chosen based on the laboratory experiments on hydraulic fracturing of the rock samples, and illustrated in Fig. 7.

For the following comparisons between the experimental and the numerical data, two cases of the experiments, which differ only in the fluid injection rates q_F and duration, are considered. Referring to Fig. 5, these comparisons consider the second injection cycle (*cycle 2*), as notches with predefined crack initiations (i.e. $d^S = 1$ at notch tips) have been applied in the FE models, which is assumed to be equivalent to the performance of *cycle 1* for enhancement of the notch. Moreover, the time at the beginning of injection in *cycle 2* has been set to zero. In the first case, the injection continues after onset of the fracture and the injection rates are give as.

$$\text{case (1): } q_F \text{ [mm}^3\text{/s]} = \begin{cases} 16.67 & : & 0\,\text{s} < t \leqslant 69\,\text{s}, \\ 1.67 & : & 69\,\text{s} < t \leqslant 284\,\text{s}, \\ 0.833 & : & 284\,\text{s} < t \leqslant 2975.5\,\text{s}, \\ 0 & : & t > 2975.5\,\text{s}. \end{cases}$$

For the second case, the injection stops upon occurrence of the crack (once the fluid pressure starts decrease in the pump) and the injection rates are.

$$\text{case (2): } q_F \text{ [mm}^3\text{/s]} = \begin{cases} 16.67 & : & 0\,\text{s} < t \leqslant 45\,\text{s}, \\ 1.67 & : & 45\,\text{s} < t \leqslant 196\,\text{s}, \\ 0.833 & : & 196\,\text{s} < t \leqslant 1102\,\text{s}, \\ 0 & : & t > 1102\,\text{s}. \end{cases}$$

For the crack initiation and propagation, the crack driving force in Eq. (42) has been adopted with $\sigma_t^S = \sigma_{crit}^S = 13.5$ MPa.

5.1. Comparison of the 2D model with the experimental results

Under the assumption of plane strains, 2D FE solutions with the geometry and boundary conditions, illustrated in Fig. 7, left, are computed. The advantage of considering a 2D solution is the ability to get a good approximation of the crack path and fluid pressure profile within a reduced calculation time in comparison with the 3D case. Quadratic shape functions are used for all variables in the FE solutions. The material parameters of the granite rocks and the injection fluid are given in Table 1. Beside this, the PFM parameters and the system compressibility $\mathcal{K}_t$ (chosen in the 2D case for simplicity as a constant), which give the best fit to the experimental results for the 2D case, are summarized in Table 2.

The comparisons between the 2D numerical solutions and the hydraulic fracture experiments in the following include the fluid pressure profiles as well as the crack radii, where the crack propagates in the model as in the experiment perpendicular to the

Table 2
Parameters of the PFM and the system compressibility for the 2D model.

Parameter	Sym.	Val.	Unit
Internal length scale	ϵ	6	mm
Residual stiffness parameter	η	10^{-3}	–
Total system compressibility	$\mathscr{K}_t$	$2\cdot10^{-7}$	$\frac{1}{Pa}\frac{kg}{m^3}$
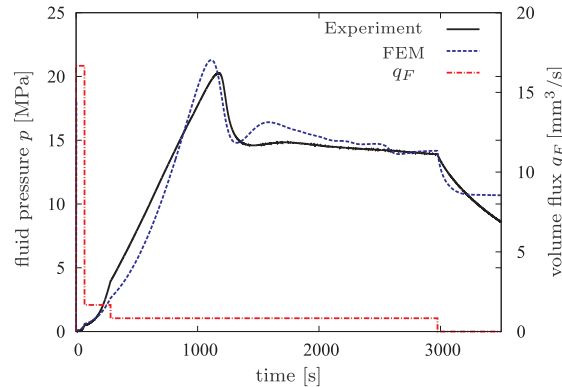
Fig. 8. A comparison between the pressure time history at the source in the 2D numerical solution and that measured in the experiment for case (1) of the fluid injection rates.

maximum confining stresses. Fig. 8 shows comparable results between the pressure time history at the source location of the FE model and that measured in the experiments for case (1) of the fluid injection rates. The relative pressure error [2] related to the maximum pressure in this case is $ERR_p \approx 5\%$.

With regards to the estimation of the crack radius in the TPM-PFM approach, we assume that $d^S = 0.5$ marks the boundary of the crack (approximation of the diffusive crack by a sharp one). The value calculated in the FE solution for case (1) is $R_c \approx 75$ mm, whereas the crack radius in the experiments for case (1) of the injection rates is, according to [68], in the range of 68–74 mm (on average, it is 71 mm), yielding a relative error of $ERR_r \approx 5\%$. The crack width, which represents the displacement jump across the crack edges, is illustrated in Fig. 9 via the vertical displacement along the sample height. This value is not measured in the experiment, however, the FE solution shows that the maximum crack width in this case is $w_c \approx 0.05$ mm.

Using the material parameters given in Table 1 as well as the parameters in Table 2, Fig. 10 shows the pressure time history at the source location of the 2D FE model compared with that measured at the pump in the experiment for case (2) of the fluid injection rates. A good agreement with regard to the pre-crack phase and the maximum pressure can be observed (the relative error related to the maximum pressure $ERR_p \approx 2\%$). In the post-crack phase, however, an increasing deviation is obtained, which can be explained based on the system compressibility and the difference in the fluid volume between the 2D model and that in the real injection system. Additionally, the crack radius in the FE model for case (2) is $R_c \approx 36$ mm and the maximum crack width in this case is $w_c \approx 0.015$ mm. The crack radius in the experiments for case (2) of injection rates is in the range of {50–54} mm (on average 52 mm), yielding a relative error in the FE simulation of $ERR_r \approx 30\%$.

### 5.2. Comparison of the 3D numerical model with the experimental results

In the following, the 3D FE solutions of the hydraulic fracture problem with the geometry illustrated in Fig. 7, right, are discussed. For the spatial discretization, tetrahedral elements with linear shape functions are used. Beside the material parameters given in Table 1, the applied model parameters, such as the internal length scale and the system compressibility (Eq. (51)), are given in Table 3.

Fig. 11 shows the crack path via the phase-field variable, which is perpendicular to the maximum confining stress. A fine mesh has been assigned at the crack path so that the grid size is smaller than half of the internal length scale ϵ, see [52]. The pressure time history at the source location of the 3D FE model (case (1) of the fluid injection rates), compared with the pressure measured at the pump in the experiment, is illustrated in Fig. 12, left. The maximum fluid pressure in the model is $P_F \approx 22$ MPa, and $P_F \approx 20.3$ MPa in the experiment, which yields a relative error of $ERR_p \approx 8\%$. Moreover, in the 3D FE model, oscillations in the pressure at the source

---

[2] $ERR_p := |(p_f - p_{ex})/p_{ex}|$: p_{ex} as the experimental value of p and p_f is the numerical one.
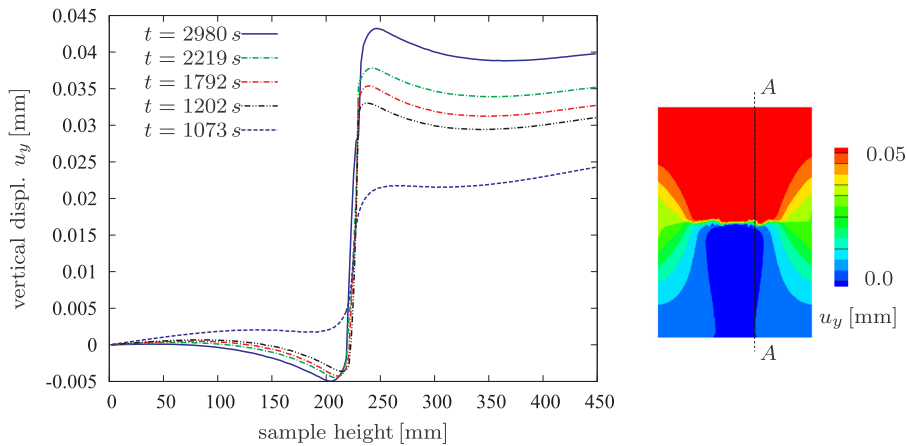
Fig. 9. Contour plot of the vertical displacement u_y at $t = 2983$ s in the 2D model (right) and displacement jumps across the crack edges at different time steps along the sample height (section A-A, 100 mm from the notch) for case (1) of the fluid injection rates (left).
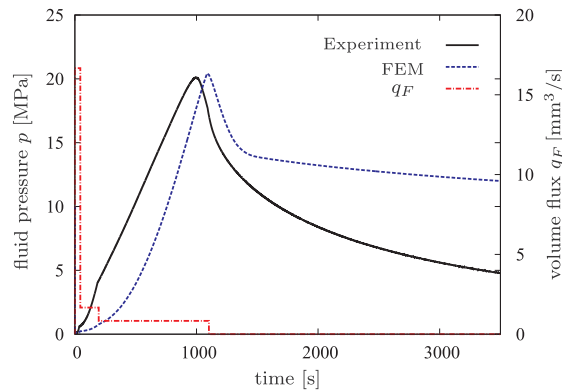
Fig. 10. A comparison between the pressure time history at the source in the 2D numerical solution and that measured in the experiment for case (2) of the fluid injection rates.

Table 3
Parameters related to the PFM and the system compressibility for the 3D FE model.

Parameter	Sym.	Val.	Unit
Internal length scale	ϵ	12	mm
Residual stiffness parameter	η	10^{-2}	–
Initial system compressibility	$\overline{\mathscr{K}}_{sys}$	$3 \cdot 10^{-11}$	$\frac{1}{\text{Pa}} \frac{\text{kg}}{\text{m}^3}$
Crit. pressure (sys. compressibility)	p_e	$2 \cdot 10^{6}$	Pa

during crack propagation due to the stepwise crack advancement are observed. During these oscillations, the FE program converges smoothly and the time steps do not become too small, proofing that the oscillations are not related to numerical instabilities. Another factor that affects the crack propagation and pressure behavior is the shape of the crack. Unlike the plane-strain 2D fracture, the crack circumference in the 3D penny-shaped fracture becomes larger after each crack advancement. Thus, for each new crack advancement, more total energy at the crack tip is needed than the previous crack step.

For estimation of the crack radius in the PFM approach, we assumes as in the 2D model that $d^S = 0.5$ marks the boundary of the crack. Thus, as illustrated in Fig. 12, right, the value of the crack radius calculated in the 3D FE model for case (1) of fluid injection is $R_c \approx 75$ mm. This value is close to the crack radii in the experiments for case (1) of injection rates, which are on average 71 mm. Thus, the relative error is $ERR_r \approx 5\%$. Moreover, the calculated maximum crack width opening is $w_c \approx 0.075$ mm.

For case (2) of the fluid injection rates and 3D FE model, the pressure time history at the source location is depicted in Fig. 13, left, and compared with the experimental data.

The maximum fluid pressure in the hydraulic fracture model $P_F \approx 23$ MPa and in the experiment $P_F \approx 20$ MPa, which yields a relative error of $ERR_p \approx 15\%$. Moreover, the estimated maximum crack radius, based on the limit $d^S = 0.5$ for the crack edges, is $R_c \approx 40$ mm (see Fig. 13, right) and the maximum crack width opening in the model is $w_c \approx 0.07$ mm. The crack radius in the
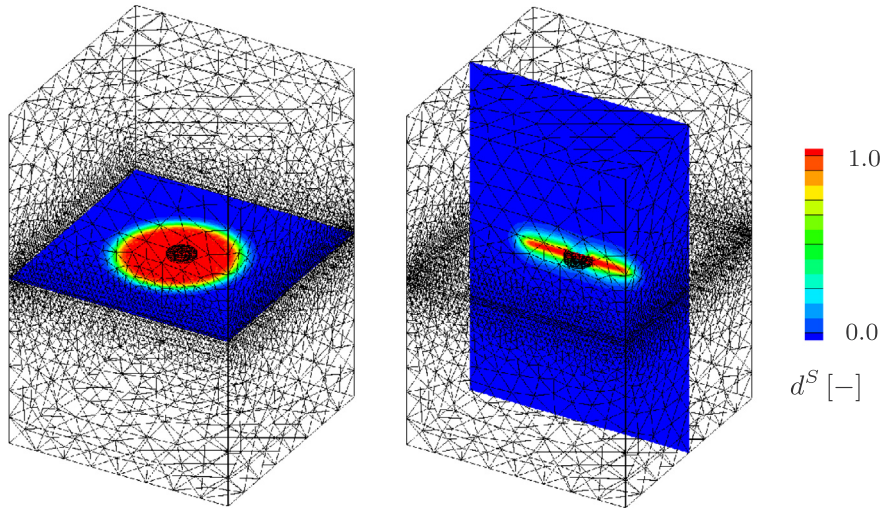
Fig. 11. Contour plots of the phase-field variable, indicating the crack radius for case (1) of the fluid injection rates.
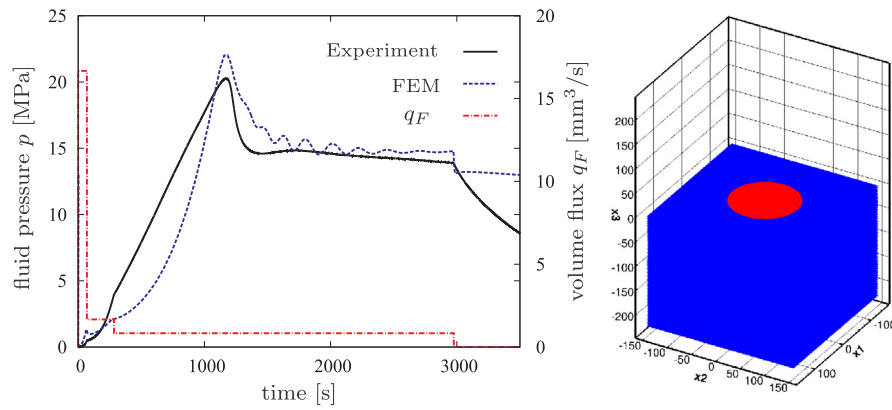

Fig. 12. Pressure time history at the source in the 3D numerical solution compared with the fluid pressure at the pump in the experiment (left) and illustration of the crack radius (right) for case (1) of the fluid injection rates.

Fig. 13. Pressure time history at the source in the 3D numerical solution compared with the fluid pressure at the pump in the experiment (left) and illustration of the crack radius (right) for case (2) of the fluid injection rates.
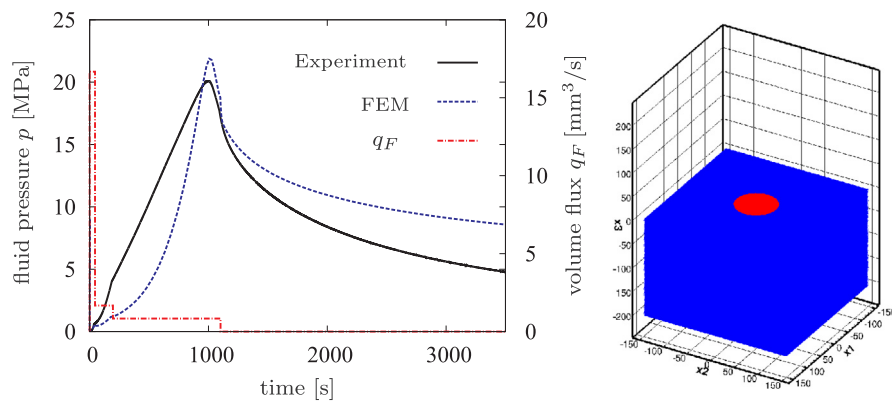
Table 4

Summary of the comparisons between the experimental data and the 2D/3D results for the two cases of the fluid injection rates q_F.

q_F		Exp.	FE-2D	*ERR* (2D)	FE-3D	*ERR* (3D)
Case (1)	P_F [MPa]	20.3	21.3	$\approx 5\%$	22	$\approx 8\%$
	R_c [mm]	71	75	$\approx 5\%$	75	$\approx 5\%$
Case (2)	P_F [MPa]	20.1	20.4	$\approx 2\%$	23	$\approx 15\%$
	R_c [mm]	52	36	$\approx 30\%$	40	$\approx 23\%$

experiments for case (2) of the injection rates is on average 52 mm, yielding a relative error in the FE simulation of $ERR_r \approx 23\%$.

5.3. Summary of the results

In Table 4, a summary of the comparisons between the 2D and 3D numerical solutions with the hydraulic fracture experimental data is presented. This includes the maximum fluid pressure P_F in the hydraulic fracturing process as well as the crack radii R_c.

Using the proposed model together with the material and model parameters, both the 2D and 3D models can predict the pressure needed to initiate the crack with good accuracy (in all cases $ERR_p \leq 15\%$). They can also be used in calculation of the crack radius, where $ERR_r \approx 5-30\%$. Qualitatively, both 2D and 3D models can predict the crack path, the pressure increase and the subsequent pressure decrease during the fracturing process.

6. Summary and conclusions

This research work presented a porous media-phase-field modeling framework with experimental calibration of hydraulic fracturing of porous brittle materials. In this, the theory of porous media was adopted for the material description on the macroscopic scale, where the formulations considered a two-phase porous material, consisting of a solid and a fluid phase (as mixture of gas and liquid). Moreover, the presentation was restricted to an isothermal, small strain regime as well as quasi-static loading conditions.

The phase-field approach, which uses a phase-field variable to distinguish between the broken and the undamaged states of the solid material and approximates the sharp crack edges by diffusive ones, was implemented in the finite element package FlexPDE. The phase-field variable was also considered in the formulations of some porous media parameters, such as the permeability and the porosity and, thus, it accounted for their permanent changes in the cracked region. In summary of the fracture initiation and propagation algorithm, a crack driving force based on the principal effective stresses and the maximum tensile stress criterion was used. In this, the cracking started when the crack driving force became greater than zero. Following this, and due to the homogeneity and isotropy assumptions, the crack started propagating stepwise perpendicular to the maximum principal stress. Due to crack opening after each step, the fluid expanded to fill the created crack space and, thus, reductions in the pressure and tensile stresses were observed. As the filling process and its speed until creating a new crack increment is governed by the fluid momentum and mass balances, the fluid viscosity, compressibility as well as the applied injection rate played the major role in the pressure time history at the source. Additionally, it has been shown that the proposed numerical algorithm and the time integration scheme lead to robust and stable numerical solutions.

Beside the numerical modeling, experimental data on hydraulic fracturing of granite rock samples were used for model calibration. In this, it has been shown through 2D and 3D boundary value problems that the numerical results yield promising qualitative and quantitative agreement with the experimental data. In this regard, the comparisons focused on the pressure time histories, the cracks radii and orientations. Future works should focus on three aspects: First, extension of the compressibility formulations in order to get a better prediction of the post-crack pressure profile. Second, inclusion of spatial variations of the heterogeneous material properties, which leads to more realistic numerical results. Third, reduction of computation time by employing, e.g. the model order reduction (MOR) methods, applying alternative time integrators as well as using advanced automated spatial adaptivity schemes based on appropriate error evaluation, related to the phase-field variable.

Appendix A. Supplementary material

Supplementary data associated with this article can be found, in the online version, at https://doi.org/10.1016/j.engfracmech. 2018.09.010.

References

[1] Adachi J, Siebrits E, Peirce A, Desroches J. Computer simulation of hydraulic fractures. Int J Rock Mech Min Sci 2007;44(5):739–57.
[2] Aldakheel F, Hudobivnik B, Hussein A, Wriggers P. Phase-field modeling of brittle fracture using an efficient virtual element scheme. Comput Methods Appl Mech Eng 2018;341:443–66.
[3] Aldakheel F, Wriggers P, Miehe C. A modified gurson-type plasticity model at finite strains: formulation, numerical analysis and phase-field coupling. Comput Mech 2017. 10.1007/s00466-017-1530-0.
[4] Allen S, Cahn J. A microscopic theory for antiphase boundary motion and its application to antiphase domain coarsening. Acta Met 1979;27:1085–95.
[5] Ambati M, Gerasimov T, Lorenzis LD. A review on phase-field models of brittle fracture and a new fast hybrid formulation. Comput Mech 2015;55:383–405.
[6] Bishop AW. The effective stress principle. Teknisk Ukeblad 1959;39:859–63.
[7] Bourdin B, Chukwudozie C, Yoshioka K. A variational approach to the numerical simulation of hydraulic fracturing. In: Proceedings of the 2012 SPE Annual Technical Conference and Exhibition (Vol. SPE 159154); 2012. doi:10.2118/159154-MS.
[8] Bourdin B, Francfort G, Marigo J. The variational approach to fracture. J Elasticity 2008;91:5–148.
[9] Bourdin B, Francfort G, Marigo J-J. Numerical experiments in revisited brittle fracture. J Mech Phys Solids 2000;48:797–826.
[10] Bowen RM. Theory of mixtures. Eringen AC, editor. Continuum Physics, vol. III. New York: Academic Press; 1976. p. 1–127.
[11] Bryant EC, Sun W. A mixed-mode phase field fracture model in anisotropic rocks with consistent kinematics. Comput Methods Appl Mech Eng 2018. https://doi.org/10.1016/j.cma.2018.08.008.
[12] Bunger AP, Gordeliy E, Detournay E. Comparison between laboratory experiments and coupled simulations of saucer-shaped hydraulic fractures in homogeneous brittle-elastic solids. J Mech Phys Solids 2013;61(7):1636–54.
[13] Cahn JW, Hilliard JE. Free energy of a nonuniform system. i. Interfacial free energy. J Chem Phys 1958;28:258–67.
[14] Cajuhi T, Sanavia L, De Lorenzis L. Phase-field modeling of fracture in variably saturated porous media. Comput Mech 2017. https://doi.org/10.1007/s00466-017-1459-3.
[15] Cao TD, Hussain F, Schrefler BA. Porous media fracturing dynamics: stepwise crack advancement and fluid pressure oscillations. J Mech Phys Solids 2018;111:113–33.
[16] Choo J, Sun W. Cracking and damage from crystallization in pores: coupled chemo-hydro-mechanics and phase-field modeling. Comput Methods Appl Mech Eng 2018;335:347–79.
[17] Clauser C, Willbrand K, Ziegler M, Feinendegen M, Siebert P, Fries T-P, Weber N. Verbundprojekt 0325167: Entwicklung eines Werkzeugs zur Auslegung von HDR-Risssystemen: Endbericht: 01. September 2010–30. Juni 2015.
[18] David S, Ruben J, Luis C. Phase field model of fluid-driven fracture in elastic media: immersed-fracture formulation and validation with analytical solutions. J. Geophys. Res.: Solid Earth 2017;122(4):2565–89.
[19] de Boer R. Theory of Porous Media. Berlin: Springer-Verlag; 2000.
[20] de Boer R, Ehlers W. The development of the concept of effective stresses. Acta Mech 1990;83:77–92.
[21] Detournay E. Mechanics of hydraulic fractures. Annu Rev Fluid Mech 2016;48(1):311–39.
[22] Diebels S. Mikropolare Zweiphasenmodelle: Formulierung auf der Basis der Theorie Poröser Medien. Habilitation, Bericht Nr. II-7, Institut für Mechanik (Bauwesen), Universität Stuttgart; 2000.
[23] Ehlers W. Foundations of multiphasic and porous materials. In: Ehlers W, Bluhm J, editors. Porous Media: Theory, Experiments and Numerical Applications. Berlin: Springer-Verlag; 2002. p. 3–86.
[24] Ehlers W, Ellsiepen P, Blome P, Mahnkopf D, Markert B. Theoretische und numerische Studien zur Lösung von Rand- und Anfangswertproblemen in der Theorie Poröser Medien, Abschlußbericht zum DFG-Forschungsvorhaben Eh 107/6. Institut für Mechanik (Bauwesen), Universität Stuttgart; 1999.
[25] Ehlers W, Luo C. A phase-field approach embedded in the theory of porous media for the description of dynamic hydraulic fracturing. Comput Methods Appl Mech Eng 2017;315:348–68.
[26] Felippa CA, Park KC, Farhat C. Partitioned analysis of coupled mechanical systems. Comput Methods Appl Mech Eng 2001;190:3247–70.
[27] Francfort G, Marigo J-J. Revisiting brittle fracture as an energy minimization problem. J Mech Phys Solids 1998;46:1319–42.
[28] Frémond M. Non-Smooth Thermomechanics. Berlin: Springer; 2002.
[29] Frémond M, Nedjar B. Damage, gradient of damage, and principle of virtual power. Int J Solids Struct 1996;33:1083–103.
[30] Griffith AA. The phenomena of rupture and flow in solids. Phil Trans Roy Soc Lond A 1921;221:163–98.
[31] Haupt P. Foundation of continuum mechanics. In: Hutter K, editor. Continuum Mechanics in Environmental Sciences and Geophysics. CISM Courses and Lectures No. 337. Wien: Springer-Verlag; 1993. p. 1–77.
[32] Heider Y. Saturated Porous Media Dynamics with Application to Earthquake Engineering. Dissertation, Report No. II-25 of the Institute of Applied Mechanics (CE), University of Stuttgart, Germany; 2012.
[33] Heider Y, Markert B. A phase-field modeling approach of hydraulic fracture in saturated porous media. Mech Res Commun 2017;80:38–46.
[34] Holbrow CH, Lloyd JN, Amato JC, Galvez E, Parks ME. Modern Introductory Physics. 2nd ed. New York: Springer; 2010.
[35] Irwin GR. Analysis of stresses and strains near the end of a crack traversing a plate. J Appl Mech 1957;24:361–4.
[36] Kraaijeveld F, Huyghe JM. Propagating cracks in saturated ionized porous media. In: de Borst R, Ramm E, editors. Multiscale Methods in Computational Mechanics. Lecture Notes in Applied and Computational Mechanics, vol. 55. Dordrecht: Springer; 2011.
[37] Kuhn C, Müller R. A continuum phase field model for fracture. Eng Fract Mech 2010;77:3625–34.
[38] Lecampion B, Bunger A, Zhang X. Numerical methods for hydraulic fracture propagation: a review of recent trends. J Nat Gas Sci Eng 2018;49:66–83.
[39] Lecampion B, Desroches J, Jeffrey RG, Bunger AP. Experiments versus theory for the initiation and propagation of radial hydraulic fractures in low-permeability materials. J Geophys Res: Solid Earth 2017;122(2):1239–63.
[40] Lee S, Mikeli A, Wheeler MF, Wick T. Phase-field modeling of proppant-filled fractures in a poroelastic medium. Comput Methods Appl Mech Eng 2016. https://doi.org/10.1016/j.cma.2016.02.008.
[41] Lee S, Wheeler MF, Wick T. Iterative coupling of flow, geomechanics and adaptive phase-field fracture including level-set crack width approaches. J Comput Appl Math 2017;314:40–60.
[42] Li L, Tang C, Li G, Wang S, Liang Z, Zhang Y. Numerical simulation of 3d hydraulic fracturing based on an improved flow-stress-damage model and a parallel FEM technique. Rock Mech Rock Eng 2012;45:801–18.
[43] Liu G, Sun W, Lowinger SM, Zhang Z, Huang M, Peng J. Coupled flow network and discrete element modeling of injection-induced crack propagation and coalescence in brittle rock. Acta Geotech 2018. https://doi.org/10.1007/s11440-018-0682-1.
[44] Mahnkopf D. Lokalisierung fluidgesättigter poröser Festkörper bei finiten elastoplastischen Deformationen. Dissertation, Bericht Nr. II-5, Institut für Mechanik (Bauwesen), Universität Stuttgart; 2000.
[45] Markert B. A constitutive approach to 3-d nonlinear fluid flow through finite deformable porous continua. Transp Porous Med 2007;70:427–50.
[46] Markert B. Weak or Strong – On Coupled Problems in Continuum Mechanics. Habilitation, Report No. II-20 of the Institute of Applied Mechanics (CE). University of Stuttgart; 2010.
[47] Markert B. A survey of selected coupled multifield problems in computational mechanics. J Coupled Syst Multiscale Dyn 2013;27:22–48.
[48] Markert B, Heider Y. Coupled multi-field continuum methods for porous media fracture. In: Mehl M, Bischoff M, Schäfer M, editors. Recent Trends in Computational Engineering - CE2014. Lecture Notes in Computational Science and Engineering, vol. 105. Springer International Publishing; 2015. p. 167–80.
[49] Markert B, Heider Y, Ehlers W. Comparison of monolithic and splitting solution schemes for dynamic porous media problem. Int J Numer Meth Eng 2010;82:1341–83.
[50] Matthies HG, Niekamp R, Steindorf J. Algorithms for strong coupling procedures. Comput Methods Appl Mech Eng 2006;195:2028–49.
[51] Miehe C, Aldakheel F, Teichtmeister S. Phase-field modeling of ductile fracture at finite strains: a robust variational-based numerical implementation of a

gradient-extended theory by micromorphic regularization. Int J Numer Meth Eng 2017;111(9):816–63.

[52] Miehe C, Hofacker M, Welschinger F. A phase field model for rate-independent crack propagation: Robust algorithmic implementation based on operator splits. Comput Method Appl M 2010;199:2765–78.

[53] Miehe C, Kienle D, Aldakheel F, Teichtmeister S. Phase field modeling of fracture in porous plasticity: a variational gradient-extended Eulerian framework for the macroscopic analysis of ductile failure. Comput Methods Appl Mech Eng 2016;312(Supplement C):3–50.

[54] Miehe C, Mauthe S, Teichtmeister S. Minimization principles for the coupled problem of Darcy–Biot-type fluid transport in porous media linked to phase field modeling of fracture. J Mech Phys Solids 2015;82:186–217.

[55] Mikelić A, Wheeler MF, Wick T. A phase-field method for propagating fluid-filled fractures coupled to a surrounding porous medium. Multiscale Model Simul 2015;13(1):367–98.

[56] Mikelić A, Wheeler MF, Wick T. A quasi-static phase-field approach to pressurized fractures. Nonlinearity 2015;28(5):1371–99.

[57] Moelans N, Blanpain B, Wollants P. An introduction to phase-field modeling of microstructure evolution. Calphad 2008;32(2):268–94.

[58] Mumford D, Shah J. Optimal approximation of piecewise smooth functions and associated variational problems. Comm Pure Appl Math 1989;42:577–685.

[59] Nguyen T, Yvonnet J, Zhu Q-Z, Bornert M, Chateau C. A phase-field method for computational modeling of interfacial damage interacting with crack propagation in realistic microstructures obtained by microtomography. Comput Methods Appl Mech Eng 2016;312(Supplement C):567–95.

[60] Obaid A, Turek S, Heider Y, Markert B. A new monolithic newton-multigrid-based FEM solution scheme for large strain dynamic poroelasticity problems. Int J Numer Meth Eng 2017;109(8):1103–29.

[61] Patil SP, Heider Y, Hernandez-Padilla C, Cruz-Chú E, Markert B. A comparative molecular dynamics-phase-field modeling approach to brittle fracture. Comput Methods Appl Mech Eng 2016;312(8):117–29.

[62] Pillai U, Heider Y, Markert B. A diffusive dynamic brittle fracture model for heterogeneous solids and porous materials with implementation using a user-element subroutine. Comput Mater Sci 2018;153:36–47.

[63] Réthoré J, de Borst R, Abellan M. A two-scale approach for fluid flow in fractured porous media. Int J Numer Meth Eng 2007;71(7):780–800.

[64] Réthoré J, de Borst R, Abellan M. A two-scale model for fluid flow in an unsaturated porous medium with cohesive cracks. Comp Mech 2008;42(2):227–38.

[65] Schanz M, Diebels S. A comparative study of Biot's theory and the linear Theory of Porous Media for wave propagation problems. Acta Mech 2003;161:213–35.

[66] Secchi S, Schrefler B. A method for 3-d hydraulic fracture simulation. Int J Fract 2012;178(1-2):245–58.

[67] Secchi S, Simoni L, Schrefler BA. Hydraulic fracturing and its peculiarities. Asia Pac J Comput Eng 2014. https://doi.org/10.1186/2196-1166-1-8.

[68] Siebert P. Laborversuche zur hydraulischen Risserzeugung in dreiaxial belasteten Granitquadern – Grundlagen, Versuchsentwicklung, – durchführung und Analyse. Dissertation. RWTH Aachen University;2017.

[69] Sneddon I. The distribution of stress in the neighbourhood of a crack in an elastic solid. Proc Roy Soc Lond A: Math Phys Eng Sci 1946;187(1009):229–60.

[70] Vandamme L, Curran JH. A three-dimensional hydraulic fracturing simulator. Int J Numer Meth Eng 1989;28(4):909–27.

[71] Weber N, Fries T-P. The XFEM with an implicit-explicit crack description for a plane-strain hydraulic fracture problem. PAMM 2013;13(1):83–4.

[72] Weber N, Siebert P, Willbrand K, Feinendegen M, Clauser C, Fries TP. The XFEM with an explicit-implicit crack description for hydraulic fracture problems. In: Bunger AP, McLennan J, Jeffrey R, editors. Effective and Sustainable Hydraulic Fracturing. Rijeka: InTech; 2013. Ch. 35, doi: 10.5772/56383.

[73] Weijers L. The near-Wellbore geometry of hydraulic fractures initiated from horizontal and deviated wells. PhD thesis. Report No. II-25 of the Institute of Applied Mechanics, Department of Civil Engineering and Geosciences. Delft University of Technology, Delft; 1995.

[74] Weinberg K, Hesch C. A high-order finite deformation phase-field approach to fracture. Continuum Mech Thermodyn 2015. https://doi.org/10.1007/s00161-015-0440-7.

[75] Willbrand K, Siebert P, Weber N, Fries T, Feinendegen M, Ziegler M, et al. Development of a numerical tool for EGS-layout calculations based on 3d XFEM fracture propagation simulations and laboratory experiments on large rock samples. In: Proceedings of the World Geothermal Congress 2015, Melbourne; 2015.

[76] Wilson ZA, Landis CM. Phase-field modeling of hydraulic fracture. J Mech Phys Solids 2016;96(Supplement C):264–90.

[77] Zienkiewicz OC, Taylor RL. The finite element method. 5th ed. The Basis vol. 1. Oxford: Butterworth Heinemann; 2000.